Electronic Supplementary Material (ESI) for Physical Chemistry Chemical Physics.
This journal is © the Owner Societies 2023

# Supporting Information: Electric-field induced second harmonic generation responses of push–pull polyenic dyes: Experimental and theoretical characterizations

Carmelo Naim,[†,‡] Raphaël Vangheluwe,[†] Isabelle Ledoux-Rak,[¶] Benoît Champagne,[§] Claire Tonnelé,[*,‡] Mireille Blanchard-Desce,[*,†] Eduard Matito,[*,‡,‖] and Frédéric Castet[*,†]

*†Univ. Bordeaux, CNRS, Bordeaux INP, ISM, UMR 5255, F-33400 Talence, France*

*‡Donostia International Physics Center (DIPC), Manuel Lardizabal Ibilbidea 4, 20018 Donostia, Euskadi, Spain*

*¶Laboratoire Lumière, Matière et Interfaces, Institut d'Alembert - ENS Paris Saclay - CNRS - CentraleSupelec, 4 avenue des Sciences 91190 -Gif-sur-Yvette - France*

*§Unité de Chimie Physique Théorique et Structurale, Chemistry Department, Namur Institute of Structured Matter, University of Namur, Belgium*

*‖Ikerbasque Foundation for Science, Plaza Euskadi 5, 48009 Bilbao, Euskadi, Spain*

E-mail: claire.tonnele@dipc.org; mireille.blanchard-desce@u-bordeaux.fr; ematito@gmail.com; frederic.castet@u-bordeaux.fr

# Contents

# 1 Synthesis

Polyenals of series **I** and **II** were obtained from the corresponding generic aldehydes via a sequential protocol based upon Wittig oxyprenylation followed by acidic hydrolysis.[S1] Synthesis of intermediate compounds **I-Pyr**[**n**] and **I-Quin**[**n**] (resp. **II-Pyr**[**n**] and **II-Quin**) was carried out by reacting **I**[**n-1**] (resp. **II**[**n-1**]) with one equivalent of **HE1** or **HE2** in anhydrous THF in the presence of a catalytic amount of 18-O-6 crown ether and 1.5 equivalent of NaH. After vigorous stirring at room temperature for 16h, a small amount of water was added to quench the NaH excess and the solvent was evaporated. The reaction mixture was dissolved in dichloromethane and washed with water. After drying the organic phase on $Na_2SO_4$, the solvent was evaporated and the crude compounds were then purified by column chromatography on silica gel eluting with a 8/2 dichloromethane/ethyl acetate mixture. The intermediate compounds **I-Pyr**[**n**] and **I-Quin**[**n**] (resp. **II-Pyr**[**n**] and **II-Quin**) were then dissolved in pure methyl iodide. After stirring for one hour, the excess MeI was evaporated and the solids were washed with ether then dried under vacuum. Compounds **A-D**[**n**] were characterized by HRMS and $^1$H NMR. Elementary analyses (EA) were also conducted for compounds **B** and **C1-3**.

**B1**

**NMR $^1$H** (200.13 MHz, $CDCl_3$): $\delta$= 9.55 (d, $J$= 6.2Hz, 1H), 8.61 (d, $J$= 8.0 Hz, 1H), 8.03 (m, 3H), 7.77-8.03 (m, 1H), 7.73 (d, $J$ = 15.4Hz, 1H), 7.64 (d, $J$=8.5Hz, 2H), 7.51 (d, $J$=15.4Hz, 1H), 6.67 (d, $J$=8.5Hz, 2H), 4.50 (s, 3H), 3.37 (m, 4H), 1.66 (m, 4H), 1.39 (m, 4H), 0.92 (t, $J$=7.0Hz, 6H). **HRMS** (LSIMS): [$C^+$] $m/z$ theo. for $C_{26}H_{33}N_2$: 373.2644, exp. : 373.2647. **EA**: % theo. for $C_{26}H_{33}N_2I+2/3\ H_2O$: C, 60.94; H, 6.75; N, 5.47, % exp.: C, 60.75; H, 6.87; N, 5.35.

**B2**

**NMR $^1$H** (200.13 MHz, $CDCl_3$): $\delta$= 9.76 (d, $J$= 6.0 Hz, 1H), 8.59 (d, $J$= 8.6 Hz, 1H), 8.08 (m, 3H), 7.93 (m, 1H), 7.93 (m, 1H), 7.69 (m, 1H), 7.47 (d, $J$= 8.6 Hz, 2H), 7.34 (d, $J$= 16,7Hz 1H), 7.05 (m, 2H), 6.67 (d, $J$= 8.4 Hz, 2H), 4.59 (s, 3H), 3.38 (t, $J$= 7.1Hz, 4H), 1.64 (m, 4H), 1.43 (m, 4H), 1.02 (t, *J*=7.1Hz, 6H). **HRMS** (LSIMS): [C +] *m/z* theo. for $C_{28}H_{35}N_2$: 399.2800, exp.: 399.2797. **EA**: % theo. for $C_{28}H_{35}N_2I + H_2O$: C, 61.76; H, 6.85; N, 5.14, % exp.: C, 61.55; H, 6.70; N, 4.96.

**B3**

**NMR $^1$H** (200.13 MHz, $CDCl_3$): $\delta$= 9.79 (d, *J*= 6.7Hz, 1H), 8.55 (d, *J*= 8.9 Hz, 1H), 8.13 (m, 3H), 7.89 (m, 1H), 7.71 (dd, *J*=14.6 Hz, *J*=11.0 Hz, 1H), 7.38 (d, *J*= 8.9Hz, 2H), 7.31 (d, *J*=14.7 Hz, 1H), 6.99 (m, 1H), 6.77 (m, 2H), 6.68-6.62(m, 1H), 6.64 (d, *J*= 9.0 Hz, 2H), 4.63 (s, 3H), 3.36 (t, *J*= 7.4Hz, 4H), 1.63 (m, 4H), 1.41 (m, 4H), 1.01 (t, *J*=7.2Hz, 6H). **HRMS** (LSIMS): [$C^+$] *m/z* theo. for $C_{30}H_{37}N_2$: 425.2957, exp.: 425.2961. **EA**: % theo. for $C_{30}H_{37}N_2I$ + 1.5 $H_2O$: C, 62.17; H, 6.96; N, 4.83, % exp.: C, 62.03; H, 6.84; N, 4.96.

**B4**

**NMR $^1$H** (200.13 MHz, $CDCl_3$): $\delta$= 9.87 (d, *J*= 6.5Hz, 1H), 8.54 (d, *J*= 8.4 Hz, 1H), 8.16 (m, 3H), 7.94 (m, 1H), 7.70 (dd, *J*=15.9 Hz, *J*=11.1 Hz, 1H), 7.35 (d, *J*= 8.9Hz, 2H), 7.32 (d, *J*=11.1 Hz,1H), 6.95 (dd, *J*=15.9 Hz, *J*=10.9 Hz, 1H), 6.77-6.61 (m, 4H), 6.63 (d, *J*= 8.9 Hz, 2H), 6.45 (dd, *J*=14.9 Hz, *J*=11.1 Hz, 1H), 4.66 (s, 3H), 3.34 (t, *J*= 7.6Hz, 4H), 1.60 (m, 4H), 1.40 (t, 4H), 1.00 (t, *J*=7.2Hz, 6H). **HRMS** (LSIMS): [$C^+$] *m/z* theo. for $C_{32}H_{39}N_2$: 451.3113, exp.: 451.3114. **EA**: % theo. for $C_{32}H_{39}N_2I + H_2O$: C, 64.42; H, 6.93; N, 4.70, % exp.: C, 64.58; H,6.79; N, 4.56.

**B5**

**NMR $^1$H** (200.13 MHz, $CDCl_3$): $\delta$= 9.86 (m, 1H), 8.54 (d, *J*= 8.8 Hz, 1H), 8.15 (m, 3H), 7.94 (m, 1H), 7.69 (dd, *J*=15.6 Hz, *J*=10.7 Hz, 1H), 7.36 (d, *J*= 8.8Hz, 2H), 7.33 (m, 4H), 6.93 (m, 1H), 6.75 (m, 3H), 6.63 (d, *J*= 9.5Hz, 2H), 6.45 (m, 1H), 4.66 (s, 3H), 3.33 (t, *J*= 7.4Hz, 4H), 1.62 (m, 4H), 1.37 (m, 4H), 0.97 (t, *J*=7.2Hz, 6H). **HRMS** (LSIMS): [$C^+$] *m/z* theo. for $C_{34}H_{41}N_2$: 477.3270, exp.: 477.3271. **EA**: % theo. for $C_{34}H_{41}N_2I + H_2O$: C, 65.59; H, 6.96; N, 4.50, % exp.: C, 65.63; H, 6.77; N, 4.08.

**C1**

**NMR $^1$H** (200.13 MHz, $CDCl_3$): $\delta$ = 8.50 (d, *J* = 6.8 Hz, 2H), 7.74 (d, *J* = 14.9 Hz, 1H), 7.54 (d, $J$= 6.8 Hz, 2H), 7.25 (d, $J$ = 4.4 Hz, 1H), 6.14 (d, $J$ = 14.9 Hz, 1H), 5.90 (d, $J$ = 4.4 Hz, 1H), 4.28 (s, 3H), 3.36 (m, 4H), 1.64 (m, 4H), 1.34 (m, 4H), 0.98 (m, 6H). **HRMS** (LSIMS): [C$^+$] $m/z$ theo. for $C_{20}H_{29}N_2S$: 329.2051, exp. : 329.2054. **EA**: % theo. for $C_{20}H_{29}IN_2S + H_2O$ : C, 50.63; H, 6.59; N, 5.90, % exp.: C, 50.83; H, 6.24; N, 5.87.

**C2**

**NMR $^1$H** (200.13 MHz, CDCl$_3$): $\delta$ = 8.63 (d, $J$ = 7.2 Hz, 2H), 7.63 (d, $J$ = 7.2 Hz, 2H), 7.47 (dd, $J$ = 14.9 Hz, $J$ = 10.9 Hz, 1H), 7.10 (d, $J$ = 14.1 Hz, 1H), 7.00 (d, $J$ = 4.2 Hz, 1H), 6.31 (d, $J$ = 14.9 Hz, 1H), 6.30 (dd, $J$ = 14.1 Hz, $J$ = 10.9 Hz, 1H), 5.80 (d, $J$ = 4.2 Hz, 1H), 4.35 (s, 3H), 3.30 (m, 4H), 1.63 (m, 4H), 1.33 (m, 12H), 0.91 (m, 6H). **HRMS** (LSIMS): [C$^+$] $m/z$ theo. for $C_{26}H_{39}N_2S$: 411.2834, exp.: 411.2831. **EA**: % theo. for $C_{26}H_{39}IN_2S$ : C, 57.98; H, 7.30; N, 5.20, % exp.: C, 57.67; H, 7.39; N, 4.93.

**C3**

**NMR $^1$H** (300.13 MHz, CDCl$_3$): $\delta$ = 8.73 (d, $J$ = 6.8 Hz, 2H), 7.69 (dd, $J$ = 15.1 Hz, $J$ = 11.4Hz, 1H), 6.88-6.80 (m, 3H), 6.85 (d, $J$ = 4.1 Hz, 1H), 6.41-6.22 (m, 4H), 4.40 (s, 3H), 3.27 (m, 4H), 1.65 (m, 4H), 1.32 (m, 12H), 0.91 (6H). NMR 13C (75.47 MHz, CDCl$_3$): $\delta$ = 160.5, 153.4, 145.5, 144.0, 143.7, 134.1, 132.9, 126.7, 124.7, 122.3, 121.5, 120.7, 102.0, 53.7, 47.6, 31.5, 27.1, 26.7, 22.6, 14.0. **HRMS** (LSIMS): [C$^+$] $m/z$ theo. for $C_{28}H_{41}N_2S$ : 437.2991, exp.: 437.2986. **EA**: % theo. for $C_{28}H_{41}IN_2S$: C, 59.56; H, 7.32; N, 4.96, % exp.: C, 59.3; H, 7.35; N, 4.79.

**C4**

**NMR $^1$H** (300.13 MHz, CDCl$_3$): $\delta$ = 8.78 (d, $J$ = 4.5 Hz, 2H), 7.73 (d, $J$ = 4.5 Hz, 2H), 7.46 (m, 1H), 6.78-6.32 (m, 8H), 5.70 (m, 1H), 4.43 (s, 3H), 3.25 (m, 4H), 1.60 (m, 4H), 1.32 (m, 12H), 0.91 (m, 6H). **HRMS** (LSIMS): [C$^+$] $m/z$ theo. for $C_{30}H_{43}N_2S$ : 463.3147, exp.: 463.3142.

**D1**

**NMR $^1$H** (200.13 MHz, CDCl$_3$): $\delta$ = 9.25 (d, $J$ = 6.9 Hz, 1H), 8.38 (d, $J$ = 8.3 Hz, 1H), 8.12 (d, $J$ = 14.5 Hz, 1H), 7.95-7.86 (m, 2H), 7.92 (d, $J$ = 6.9 Hz, 1H), 7.73 (m, 1H), 7.48

(d, $J$ = 4.4 Hz, 1H), 6.87 (d, $J$ = 14.5 Hz, 1H), 6.05 (d, $J$ = 4.4 Hz, 1H), 4.40 (s, 3H), 3.42 (m, 4H), 1.66 (m, 4H), 1.34 (m, 12H), 0.93 (m, 6H). **HRMS** (LSIMS): [$C^+$] $m/z$ theo. for $C_{28}H_{39}N_2S$ : 435.2834, exp.: 435.2841.

**D2**

**NMR $^1$H** (200.13 MHz, $CDCl_3$): $\delta$ = 9.49 (d, $J$ = 7.2 Hz, 1H), 8.38 (d, 8.3 Hz, 1H), 7.98 (d, $J$ = 7.2 Hz, 1H), 7.94 (m, 2H), 7.78 (m, 2H), 7.11 (d, $J$ = 4.6 Hz, 1H), 7.08 (m, 2H), 6.52 (m, 1H), 5.91 (d, $J$ = 4.6 Hz, 1H), 4.48 (s, 3H), 3.36 (t, 4H), 1.62 (m, 4H), 1.34 (m, 12 H), 0.92 (m, 6H). **HRMS** (LSIMS): [$C^+$] $m/z$ theo. for $C_{30}H_{41}N_2S$: 461.2991, exp.: 461.2992.

**D3**

**NMR $^1$H** (300.13 MHz, $CDCl_3$): $\delta$ = 9.61 (d, $J$ = 6.8 Hz, 1H), 8.40 (d, $J$ = 8.3 Hz, 1H), 8.02 (m, 2H), 7.83 (m, 2H), 7.70 (m, 1H), 7.10 (d, $J$ = 14.9Hz, 1H), 6.90 (m, 3H), 6.53 (dd, $J$= 14.1Hz, $J$= 11.2 Hz, 1H), 6.30 (dd, $J$= 14.1Hz, $J$= 11.2 Hz, 1H), 5.80 (6.53 (d, $J$= 4.0Hz, 1H), 4.55 (s, 3H), 3.32 (m, 4H), 1.52 (m, 4H), 1.40 (m, 12H), 0.92 (m, 6H). **HRMS** (ESI): [$C^+$] $m/z$ theo. for $C_{32}H_{43}N_2S$: 487.31415, exp.: 487.31239.

**D4**

**NMR $^1$H** (300.13 MHz, $CDCl_3$): $\delta$ = 9.69 (d, $J$ = 6.6Hz, 1H), 8.38 (d, $J$ = 8.3 Hz, 1H), 8.00 (m, 3H), 7.80 (d, $J$ = 4.8 Hz, 1H), 7.60 (dd, $J$= 14.1Hz, $J$= 11.2 Hz, 1H), 7.16 (m, 3H), 6.87 (d, $J$ = 3.9 Hz, 1H), 6.62 (m, 4H), 5.65 (d, $J$= 3.9Hz, 1H), 4.50 (s, 3H), 3.23 (m, 4H), 1.62 (m, 4H), 1.34 (m, 12H), 0.93 (m, 6H). **HRMS** (ESI): [$C^+$] $m/z$ theo. for $C_{34}H_{45}N_2S$: 513.32980, exp.: 513.32818. **EA**: % theo. for $C_{34}H_{45}IN_2S$: C, 61.15; H, 7.24; N, 4.19; S, 4.80, % exp.: C, 61.23; H, 6.88; N, 4.52; S, 4.91

**D5**

**NMR $^1$H** (600 MHz, DMSO-d6): $\delta$ = 9.15 (d, $J$=6.5Hz, 1H), 8.77 (d, $J$=8.4Hz, 1H), 8.36 (d, $J$=8.8Hz, 1H), 8.30 (s, 1H), 8.20 (m, 1H), 8.21 (m, 3H), 7.72 (d, $J$=14.2Hz, 1H), 6.97 (m, 1H), 6.84 (s, 1H), 6.77 (m, 2H), 6.59 (m, 1H), 6.50 (m, 1H), 6.40 (m, 1H), 6.23 (m, 1H), 5.79 (s, 1H), 4.46 (s, 3H), 3.32 (m, 4H), 1.56 (m, 4H), 1.28 (m, 12H), 0.87 (m, 6H). **HRMS** (ESI): [$C^+$] $m/z$ theo. for $C_{36}H_{47}N_2S$: 539.34545, exp.: 539.34368.

# 2 Definition of the geometrical parameters

## 2.1 Bond length alternation

The bond length alternation (BLA) along the conjugated polyenic bridge connecting the donor and acceptor units is calculated as:

$$BLA = \frac{1}{N-2}\sum_{i=1}^{N-2}(-1)^{i+1}(d_{i+1,i+2} - d_{i,i+1}) \tag{1}$$

where $N$ is the total number of carbon atoms in the $\pi$-conjugated chain and $d_{i,j}$ is the interatomic distance between carbons $i$ and $j$. According to the 2-state resonance picture schematized in Figure S1 for **D3**, a negative (positive) value of the BLA calculated along the $C_1$-$C_8$ chain indicates that the ground-state electronic structure is dominated by structure 1 (2). A value equal to zero indicates that the two resonance forms equivalently contribute to the ground state.

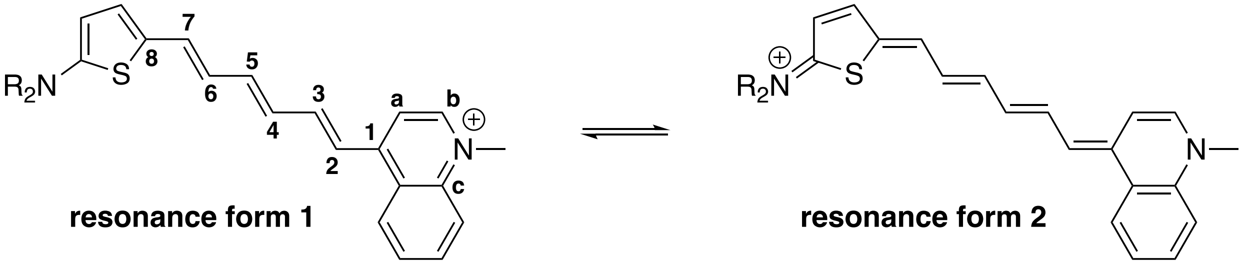

Figure S1: Resonance structures of **D3** and labels of atoms (1-8) used to calculate the bond length alternation.

## 2.2 Torsional angles

Table S1: Definition of the dihedral angles $\theta_1$-$\theta_8$ schematized in Figure S2b. See Figure S1 for atom labels.

| Angle | atoms |
|---|---|
| $\theta_1$ | S-C-N-$C_{But}$ |
| $\theta_2$ | a-1-2-3 |
| $\theta_3$ | 6-7-8-S |
| $\theta_4$ | 1-2-3-4 |
| $\theta_5$ | 5-6-7-8 |
| $\theta_6$ | 2-3-4-5 |
| $\theta_7$ | 4-5-6-7 |
| $\theta_8$ | 3-4-5-6 |

# 3 Derivation of an optimal force field for the D3 dye

## 3.1 Iterative parameterization of bond lengths and torsional potentials

At the DFT level, the BLA along the polyenic bridge amounts to -0.043 Å while the original GAFF (Generalized Amber Force Field) relaxed geometry yields a value of -0.054 Å due to the limited number of atom types used (ca and c2). Besides, the planarity of the DFT structure is not well reproduced, with out-of-plane deviations of up to 14°. These discrepancies in the molecular structure with respect to DFT expectedly translate into poor estimations of the first hyperpolarizability, namely $\beta_{tot}$(GAFF) = 2.269 $10^5$ a.u. against 1.924 $10^5$ a.u. with the reference DFT geometry.

To achieve a more accurate description of the molecular geometry, we derived new parameters for both bonds and torsional potentials using a simplified structure of the **D3** molecule, in which butyl chains were removed from the chromophore and replaced by methyl groups (Figure S2). Practically, several new atom types were added to the original GAFF (Figure S2a) to properly reproduce the bond lengths and thus, the BLA. The torsional potentials around the dihedral angles $\theta_1$-$\theta_5$ were fitted on relaxed potential energy scans performed at the M06-2X/6-311G(d) level in the gas phase (Figure S3). The FF potentials are free-energy profiles obtained using the adapting biasing force (ABF) method considering the chromophore inside a box with 40 Ar atoms at the temperature of 298.15 K. Note that the torsional potentials around the $\theta_6$-$\theta_8$ angles were described using standard GAFF in all MD simulations. Parameters for bonds and torsions were derived iteratively and converged values were used as starting point to describe the whole **D3** molecule, including butyl chains. A final refinement of the bonds was done so as to reproduce accurately the DFT geometry of the whole system and proper description of the dihedrals was checked.

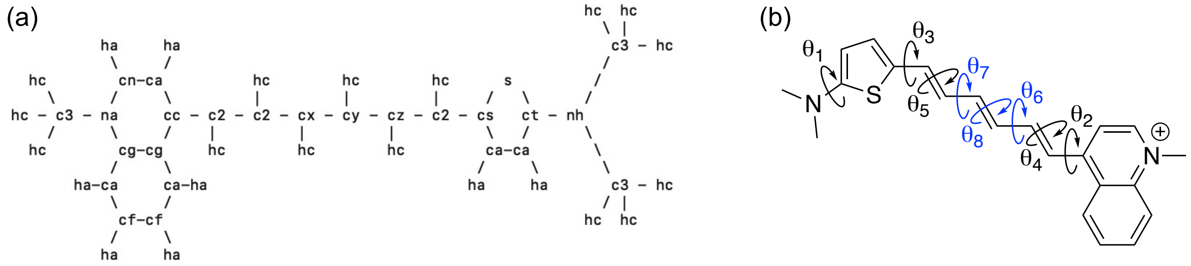

Figure S2: Geometry of the fragment employed in the optimization of the AMBER force field. (a) Atom types defined in the modified GAFF, (b) The reparameterized dihedrals are $\theta_{1-5}$. The torsional potentials around $\theta_6$-$\theta_8$ (in blue) were not reparameterized.

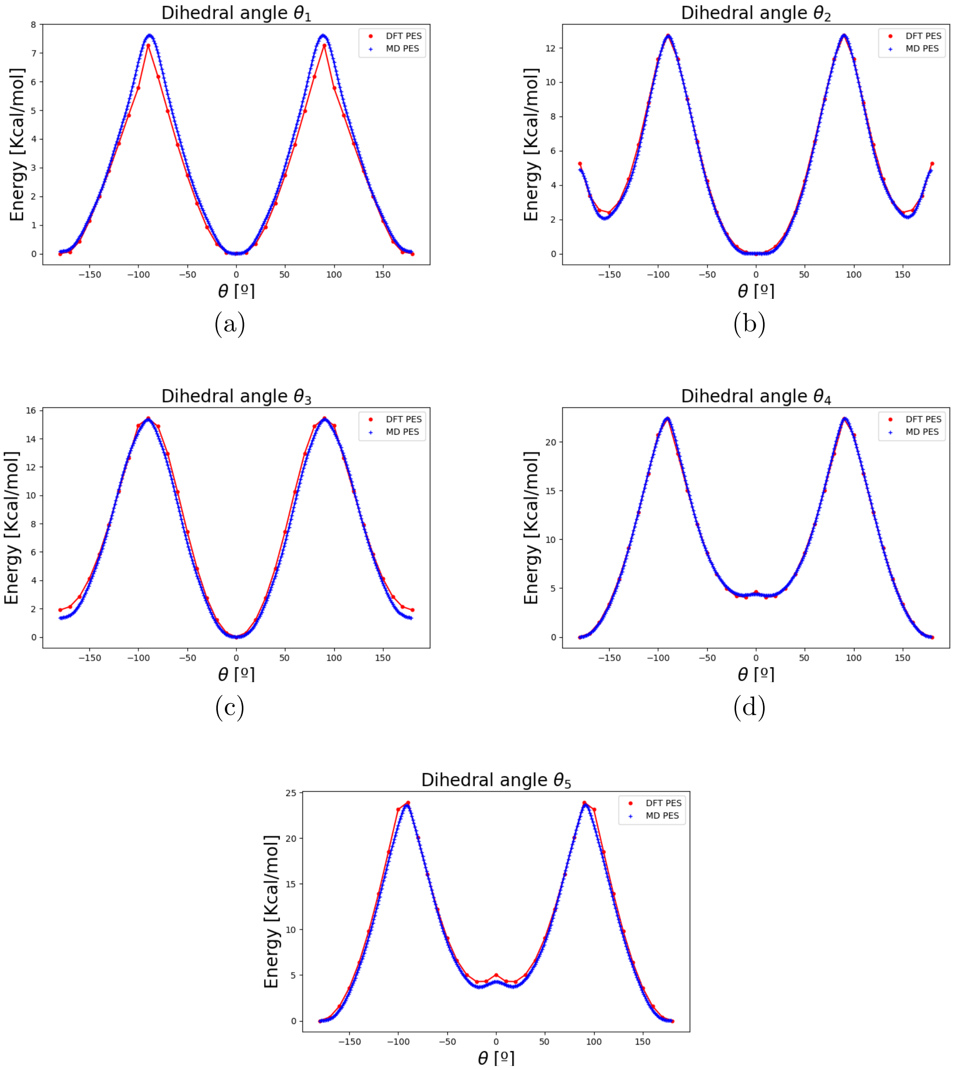

(a) (b) (c) (d) (e)

Figure S3: Relaxed potential energy scans calculated at the M06-2X/6-311G(d) level (red) and force field fitted potentials (blue) for the **D3** dye.

## 3.2 Assessment of the quality of the modified force field

In order to assess the quality of the reparameterized force field, the geometry of the **D3** molecule was optimized using molecular mechanics (MM) with the original and system-specific derived force fields and compared to the geometry optimized using the reference DFT level. Results gathered in Table S3 show that MM calculations using the reparameterized GAFF reproduce well the BLA along the $\pi$-conjugated bridge, while they give rise to a slightly less planar structure compared to DFT, with differences in the $\theta_2$ and $\theta_5$ dihedrals of the order of 10°. Note that the deviation from planarity resulting from the MM optimization is canceled out by the subsequent MD simulations, which predict a strictly planar average structure (Table S4).

Table S2: Values of the bond distances $d_{ij}$ and BLA (Å), and of dihedrals (degrees) optimized at the DFT and MM levels with the original and reparameterized GAFF for the **D3** chromophore. Absolute differences with DFT values are also reported.

| Parameters | DFT | MM (GAFF rep.) | Diff. | MM (GAFF orig.) | Diff. |
|---|---|---|---|---|---|
| $d_{12}$ | 1.424 | 1.423 | -0.001 | 1.506 | 0.082 |
| $d_{23}$ | 1.372 | 1.373 | 0.001 | 1.334 | -0.038 |
| $d_{34}$ | 1.411 | 1.411 | 0.000 | 1.332 | -0.079 |
| $d_{45}$ | 1.372 | 1.374 | 0.002 | 1.330 | -0.042 |
| $d_{56}$ | 1.412 | 1.411 | -0.001 | 1.331 | -0.081 |
| $d_{67}$ | 1.370 | 1.371 | 0.001 | 1.333 | -0.036 |
| $d_{78}$ | 1.415 | 1.416 | 0.001 | 1.490 | 0.075 |
| BLA | -0.043 | -0.041 | 0.002 | -0.054 | -0.011 |
| $\theta_1$ | 1.4 | 4.6 | 3.3 | -4.6 | 3.2 |
| $\theta_2$ | 2.8 | 14.0 | 11.2 | 16.9 | 14.1 |
| $\theta_3$ | -178.9 | -176.8 | 2.0 | -179.9 | 1.1 |
| $\theta_4$ | -179.3 | 179.7 | 0.4 | 179.8 | 0.6 |
| $\theta_5$ | 179.9 | 171.8 | 8.0 | 180.0 | 0.1 |
| $\theta_6$ | -179.3 | -179.3 | 0.1 | -179.3 | 0.0 |
| $\theta_7$ | 179.8 | 179.0 | 0.8 | 179.9 | 0.1 |
| $\theta_8$ | 179.9 | 179.4 | 0.5 | 179.9 | 0.0 |

To assess the impact of the geometry mismatches on the NLO responses, $\beta_{tot}$ has been computed at the IEF-PCM/M06-2X/6-311+G(d) level by using both the DFT and MM geometries (Table S3). Using the MM structure optimized with the original GAFF provides a $\beta_{tot}$ value overestimated by more than 15%, while the overestimation is reduced to about 7% with the reparameterized force field. Note that fixing all dihedral angles to their DFT-optimized values only slightly reduces the overestimation of $\beta_{||}$, indicating that the difference can only be partly ascribed to the deviation from planarity of the MM geometry.

Table S3: Static $\beta_{tot}$ values (a.u.) calculated at the IEF-PCM/M06-2X/6-311+G(d) level in chloroform using the DFT and MM geometries, and using the MM geometry while fixing all dihedral angles listed in Table S2 to their DFT-optimized values. Deviations (in %) with respect to values computed using the DFT geometry are listed in the last column.

| Geometry | $\beta_{tot}(0;0,0)$ | % wrt DFT |
|---|---|---|
| DFT | 1.92E+05 | - |
| MM (GAFF original) | 2.27E+05 | 15.2 |
| MM (GAFF reparameterized) | 2.08E+05 | 7.3 |
| MM (GAFF rep. + DFT dihedrals) | 2.05E+05 | 6.0 |

### 3.3 Assessment of the quality of the force field used for chloroform

The quality of the solvent description using standard GAFF parameters and DFT-derived charges has been verified by comparing the calculated mass density with the experimental one (1.468 g/cm$^{-3}$). For this purpose we performed an NpT simulation on 1600 chloroform molecules at 1 atm and 298.15 K obtaining a density of 1.415 g/cm$^{-3}$.

## 4 MD simulations on the D3/iodide complex

### 4.1 Probability distributions of geometrical parameters

The distributions of different geometrical parameters characterizing the **D3**/iodide complex have been calculated for the 20000 frames extracted from each NVT simulation starting at two different initial values of the dihedral $\theta_3$, *i.e.* for 40000 geometrical structures. Namely, the distributions of i) the dihedral angles $\theta_i$ along the $\pi$-conjugated linker, ii) the average bond length alternation (BLA), iii) the average distance ($d_{NI}$) between the counterion $I^-$ and the nitrogen of the quinolinium group and iv) the dihedral angle $\theta_{PhI}$ between the terminal phenyl and the anion are reported in Figures S4, S5, S7, S8 and S9, respectively. They are compared to the distributions obtained using the 400 geometries used for computing the NLO properties. The average values of the geometrical parameters, extracted from the full and reduced sets of structures, are reported in Table S4. The correlation of the results show that the 400 snapshots selected for calculating the NLO properties are representative of the dynamics of the system.

Table S4: Values of geometrical parameters of the **D3**/iodide complex (BLA and $d_{NI}$ in Å, and dihedral angles $\theta_i$ in degrees) averaged over 40000 structures and over the 400 snapshots selected for calculation of the NLO properties.

| Property | MD (40000 snapshots) | MD (400 snapshots) |
|---|---|---|
| BLA | -0.042 ± 0.022 | -0.045 ± 0.023 |
| $d_{NI}$ | 4.56 ± 0.48 | 4.57 ± 0.47 |
| $\theta_1$ | -0.4 ± 14.1 | 0.4 ± 12.9 |
| $\theta_2$ | 0.0 ± 14.1 | -0.7 ± 14.6 |
| $\theta_3$ (sim 1) | 180.1 ± 11.1 | 180.1 ± 10.1 |
| $\theta_3$ (sim 2) | 0.0 ± 9.4 | -0.3 ± 10.5 |
| $\theta_4$ | 180.0 ± 8.9 | 180.4 ± 8.8 |
| $\theta_5$ | 180.0 ± 10.2 | 179.4 ± 10.5 |
| $\theta_6$ | 180.0 ± 6.3 | 180.3 ± 6.5 |
| $\theta_7$ | 180.0 ± 6.1 | 179.9 ± 6.1 |
| $\theta_8$ | 180.0 ± 6.4 | 180.2 ± 6.3 |
| $\theta_{PhI}$ | 177.5 ± 39.3 | 175.1 ± 45.9 |

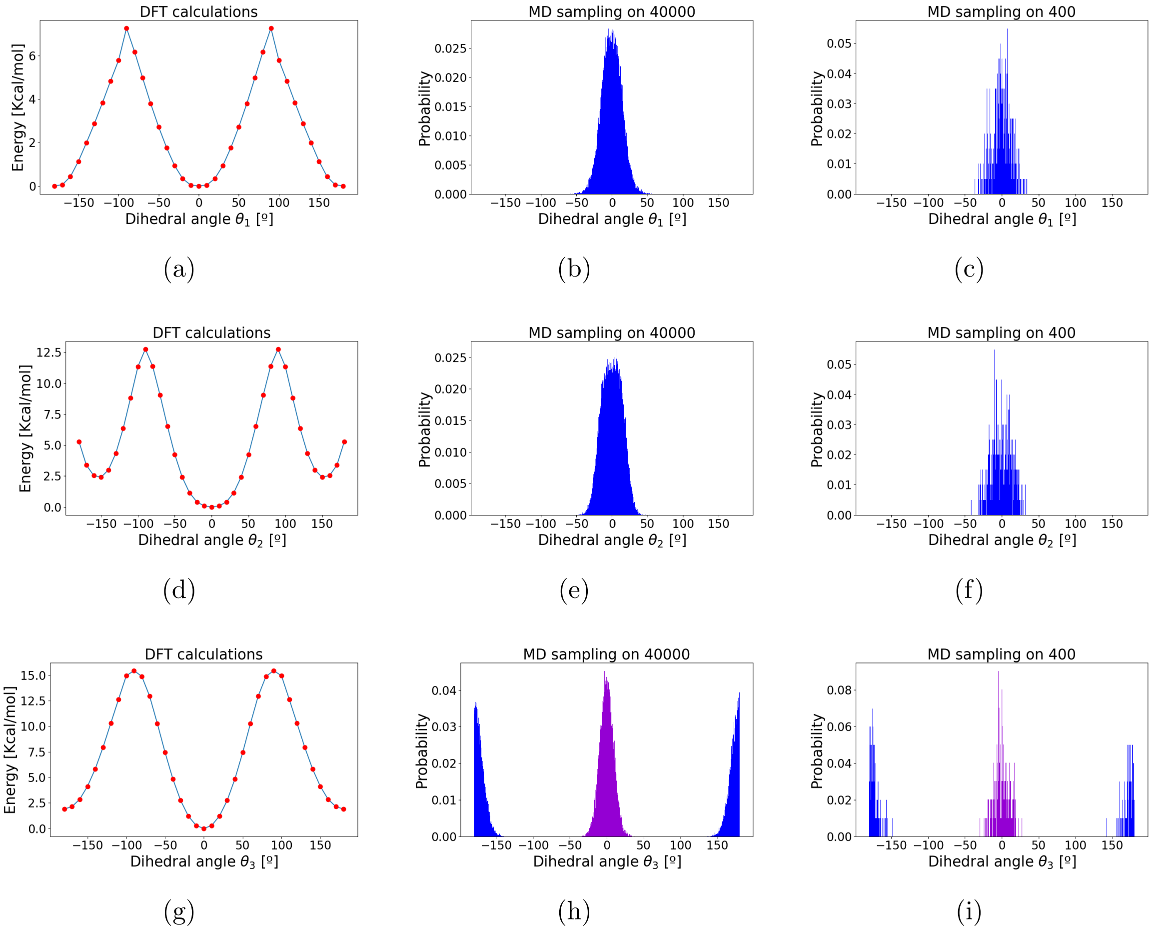

(a) (b) (c)

(d) (e) (f)

(g) (h) (i)

Figure S4: Potential energy curves associated to the rotation of the dihedrals $\theta_1$, $\theta_2$ and $\theta_3$ in **D3** (left), and probability distributions of $\theta_1$, $\theta_2$ and $\theta_3$ in the **D3**/iodide complex obtained using 40000 structures (middle) and the selected 400 structural snapshots (right) extracted from the MD trajectories. The two colors in the distributions of $\theta_3$ (plots (h) and (i)) correspond to two different trajectories starting from $\theta_3 = 0°$ (purple) and $\theta_3 = 180°$ (blue).

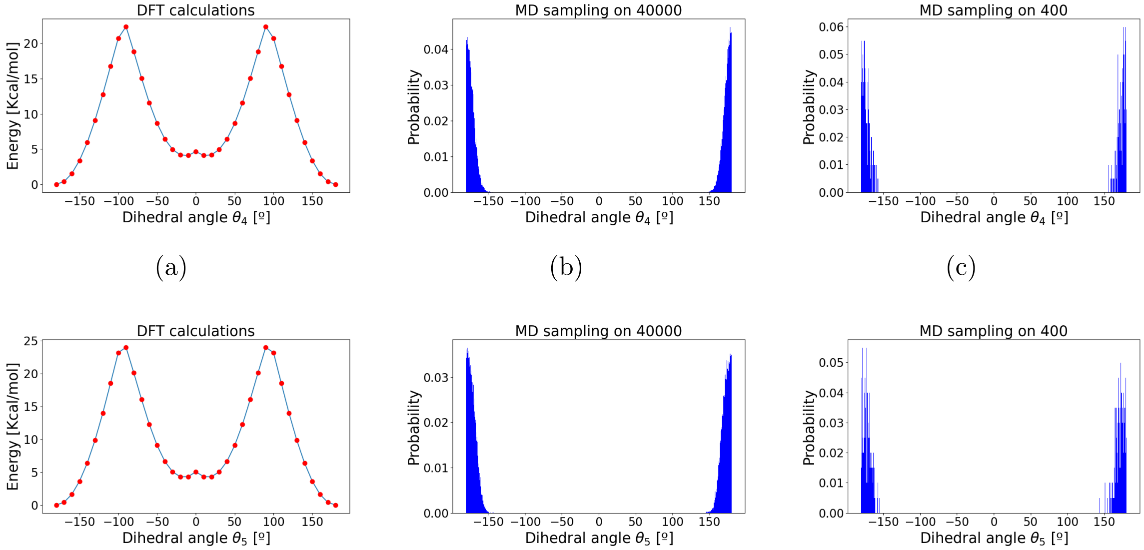

(a) (b) (c)

(d) (e) (f)

Figure S5: Potential energy curves associated to the rotation of the dihedrals $\theta_4$ and $\theta_5$ in **D3** (left), and probability distributions of $\theta_4$ and $\theta_5$ in the **D3**/iodide complex obtained using 40000 structures (middle) and the selected 400 structural snapshots (right) extracted from the MD trajectories.

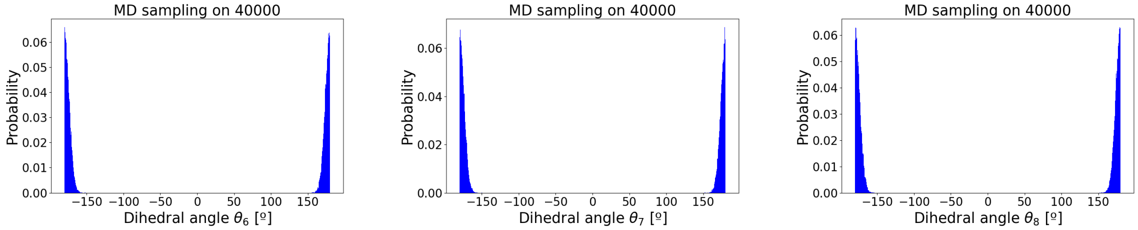

(a) (b) (c)

Figure S6: Probability distributions associated to the rotation around the internal dihedrals $\theta_6$, $\theta_7$ and $\theta_8$ of **D3** in the **D3**/iodide complex.

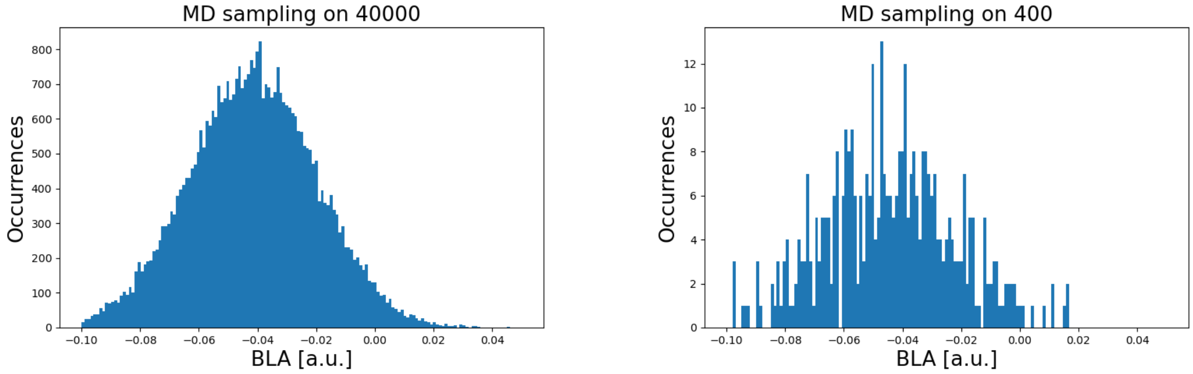

(a) (b)

Figure S7: Probability distributions of the BLA along the conjugated bridge of **D3** in the **D3**/iodide complex, obtained using 40000 structures (left) and the selected 400 structural snapshots (right) extracted from the MD trajectories.

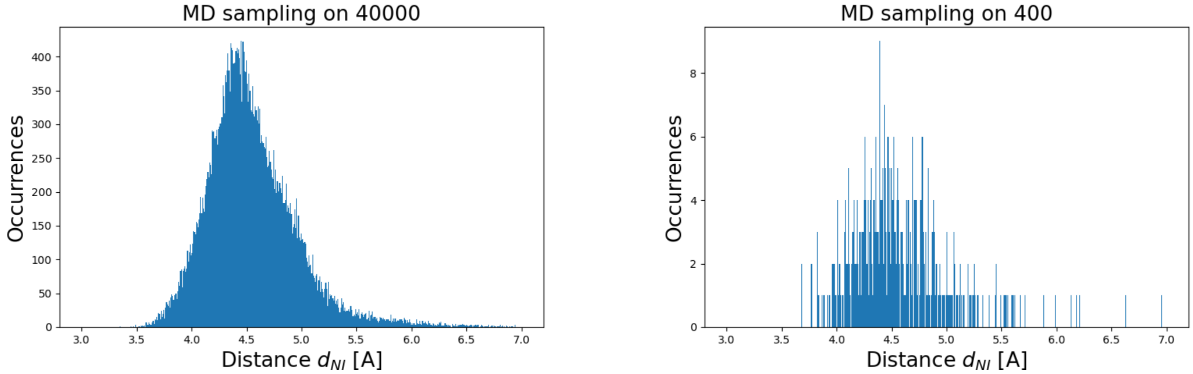

(a) (b)

Figure S8: Probability distributions of the distances between the nitrogen of the quinolinium group and the iodine atom in the **D3**/iodide complex, obtained using 40000 structures (left) and the selected 400 structural snapshots (right) extracted from the MD trajectories.

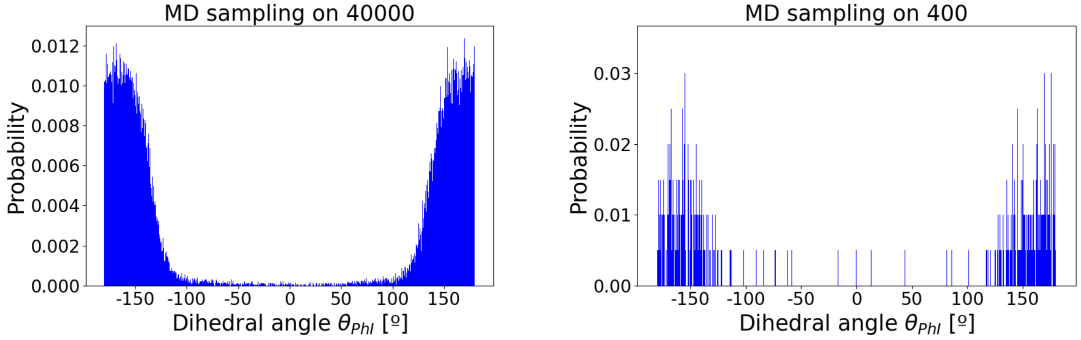

(a) (b)

Figure S9: Probability distributions of the dihedral angle $\theta_{PhI}$ = (I-b-N-c) (see Figure S1 for atom labels) in the **D3**/iodide complex, obtained using 40000 structures (left) and the selected 400 structural snapshots (right) extracted from the MD trajectories.

## 4.2 Time evolution of the EFISH properties over the MD trajectories

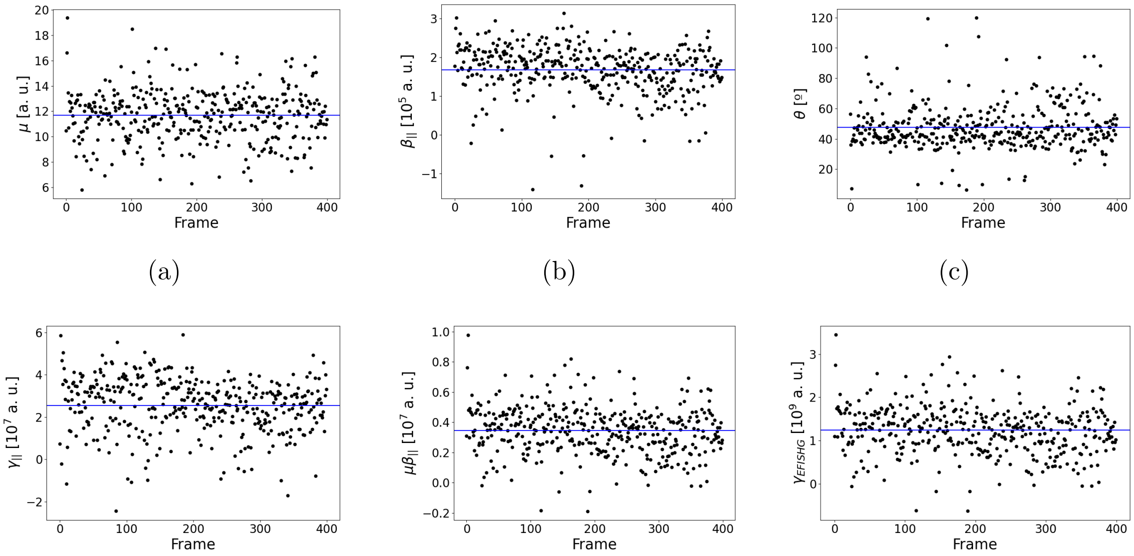

(a) (b) (c)

(d) (e) (f)

Figure S10: Time evolution along the MD trajectories of the EFISH properties of the **D3**/iodide complex.

## 4.3 Structure - NLO properties relationships

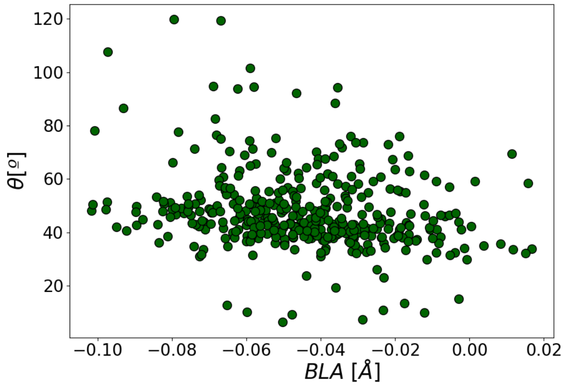

Figure S11: Evolution of the $\theta$ angle (degrees) between the $\vec{\mu}$ and $\vec{\beta}$ vectors with respect to the bond length alternation (Å) in the **D3**/iodide complex.

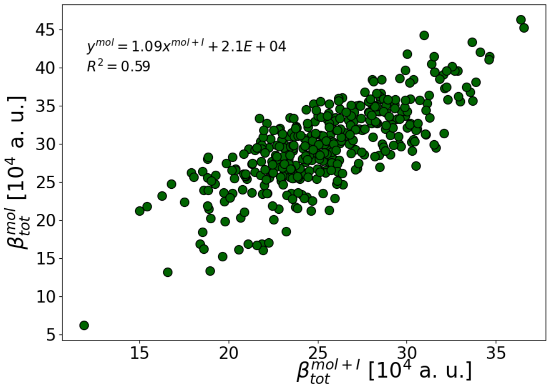

Figure S12: Evolution of $\beta_{tot}$ values (in $10^4$ a.u.) calculated for the **D3**/iodide complex with respect to those calculated for the same geometries of the **D3** chromophore only (after removing the anion).

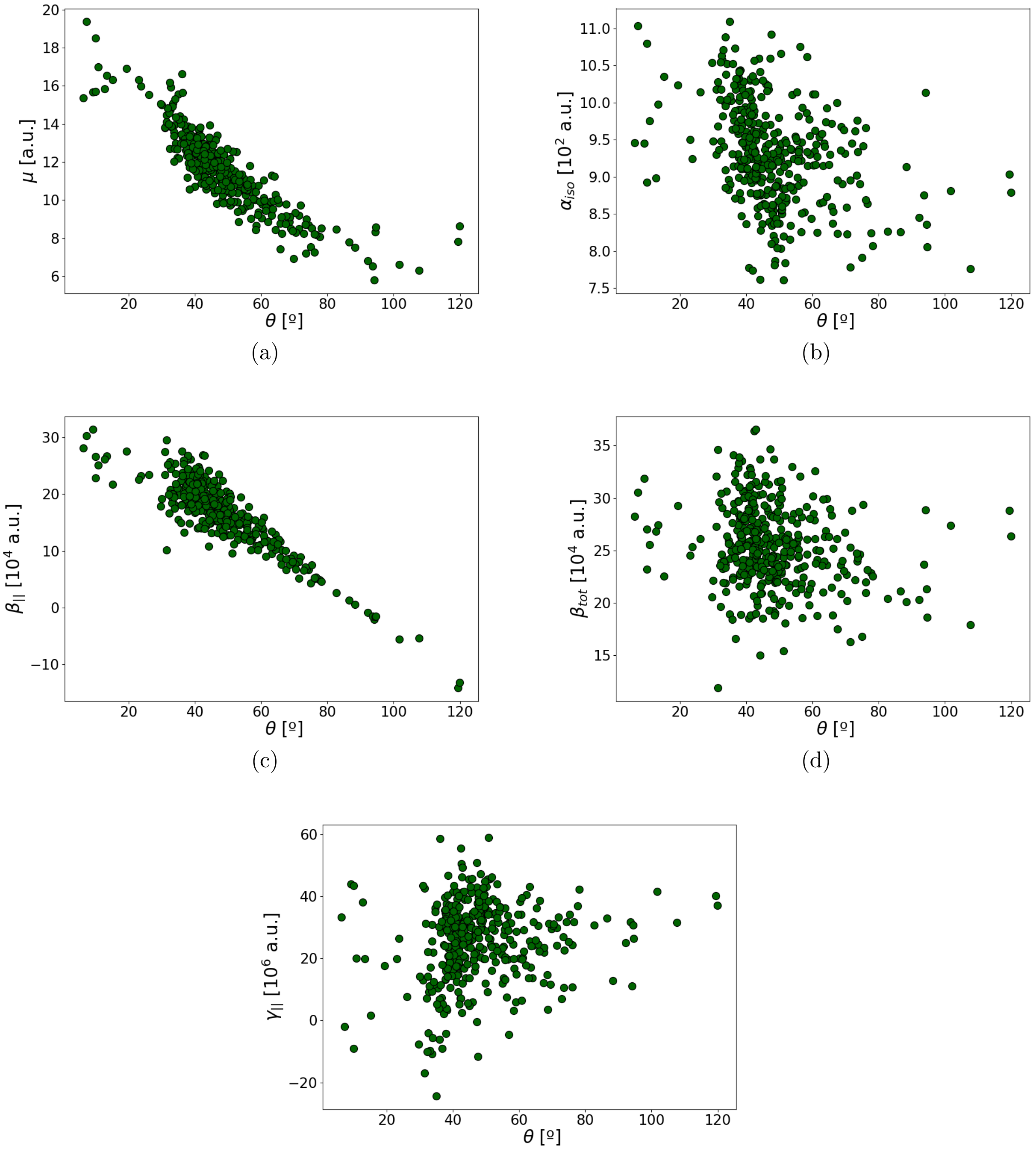

(a) (b)

(c) (d)

(e)

Figure S13: Evolution of the optical quantities with respect to the $\theta$ angle (degrees) between the $\vec{\mu}$ and $\vec{\beta}$ vectors in the **D3**/iodide complex: (a) dipole moment (a.u.), (b) isotropic polarizability ($\alpha_{iso}$, a.u.), $\beta_{||}$ ($10^4$ a.u.), $\beta_{tot}$ ($10^4$ a.u.), and $\gamma_{||}$ ($10^7$ a.u.).

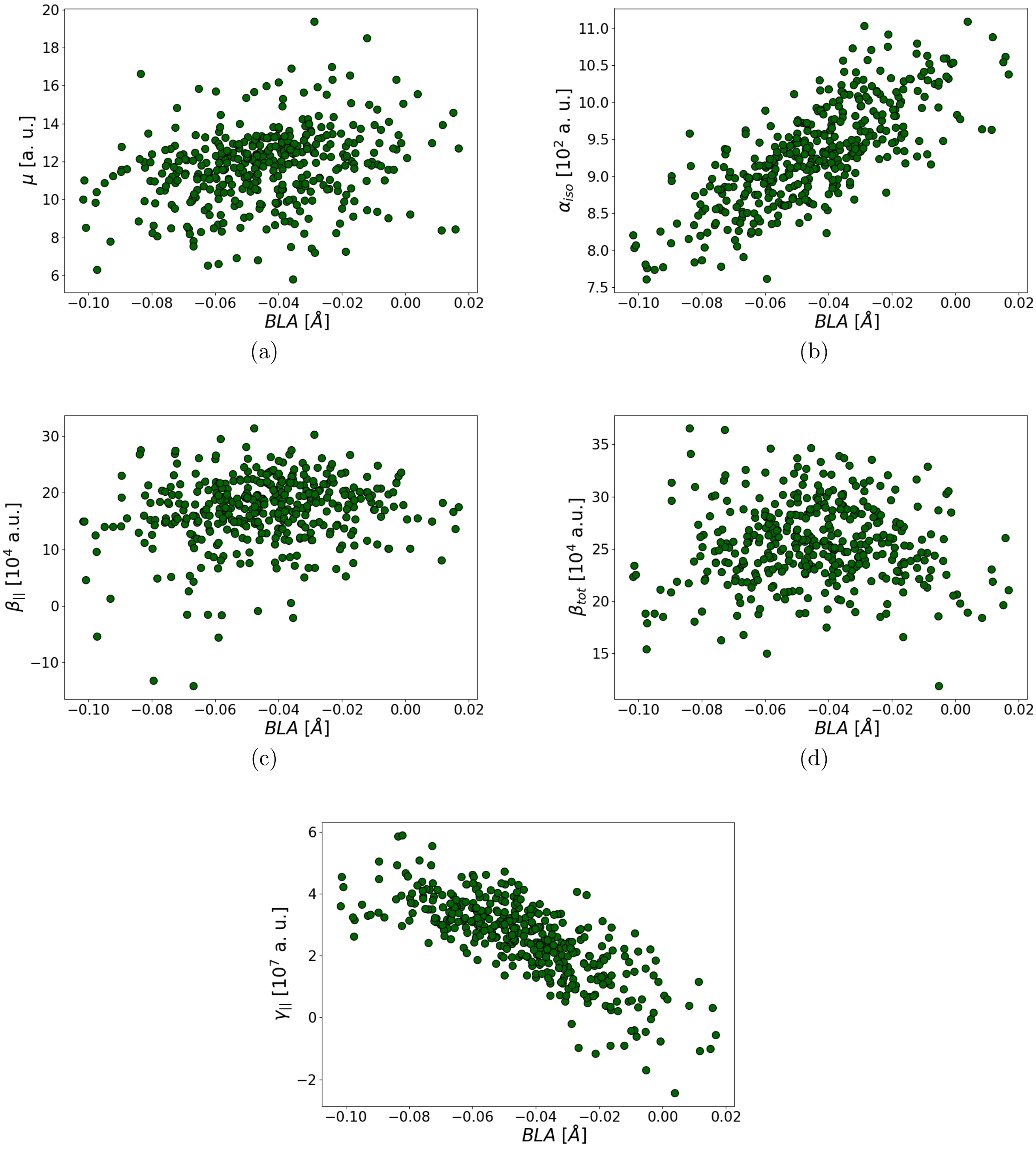

(a)

(b)

(c)

(d)

(e)

Figure S14: Evolution of the optical quantities with respect to the bond length alternation (Å) in the **D3**/iodide complex: (a) dipole moment (a.u.), (b) isotropic polarizability ($\alpha_{iso}$, a.u.), $\beta_{||}$ ($10^4$ a.u.), $\beta_{tot}$ ($10^4$ a.u.), and $\gamma_{||}$ ($10^7$ a.u.).

# 5 Assessment of the DFT approximation for computing NLO properties

## 5.1 Performance of M06-2X with respect to MP2

To assess the reliability of the selected exchange-correlation functional, the static first hyperpolarizabilities $\beta_{tot}$ of compounds of series **D** were calculated at the M06-2X/6-311+G(d) level (in vacuum) and compared to MP2 calculations carried out with the same basis set. As shown in Figure S15, the very good correlation observed for the two sets of values validates the suitability of the M06-2X exchange-correlation functional for the series of investigated systems.

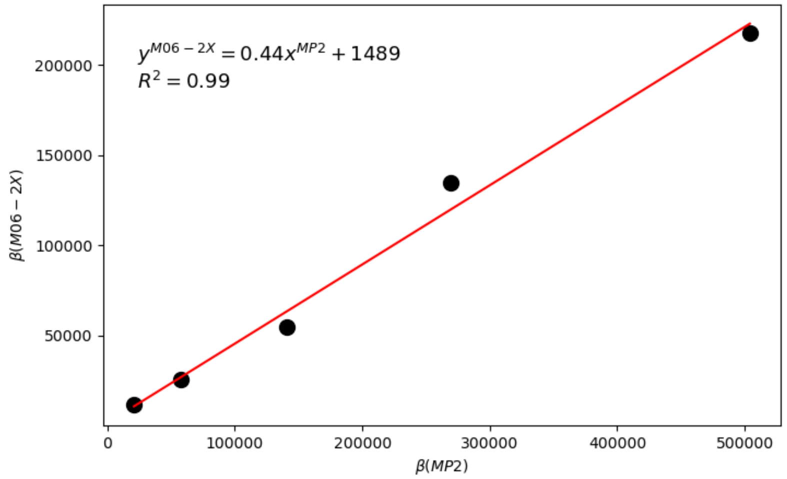

Figure S15: Comparison of static first hyperpolarizabilities ($\beta = \beta_{tot}$, in a.u.) of compounds of series **D**, computed at the M06-2X and MP2 levels using the 6-311+G(d) basis set. The geometries of the compounds have been optimized at the IEF-PCM/M06-2X/6-311+G(d) level.

## 5.2 Impact of the basis set

Three basis sets of increasing size (6-311+G(d), aug-cc-pVDZ and aug-cc-pVTZ) have been tested for molecules of series **D**, by calculating their static first hyperpolarizabilities at the

M06-2X level. The results displayed in Figure S16 show that the two smaller basis sets (6-311+G(d) and aug-cc-pVDZ) provide similar results to the ones obtained using aug-cc-pVTZ, validating the choice of 6-311+G(d) for the calculation of the NLO properties of the dyes.

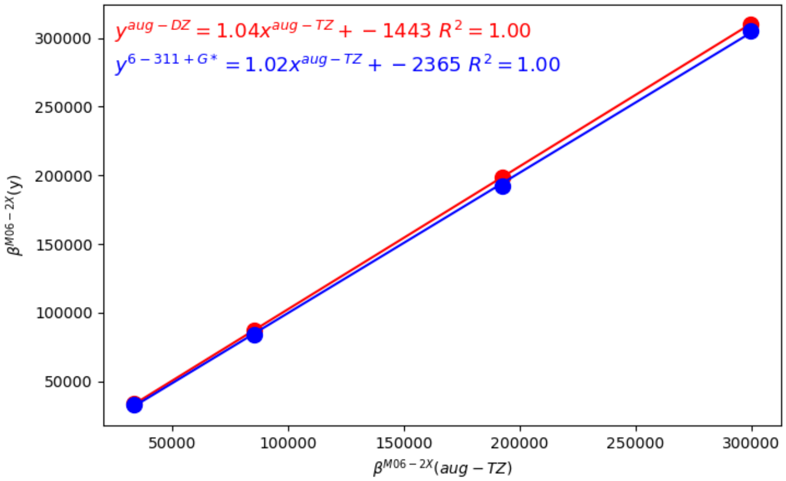

Figure S16: Comparison of static first hyperpolarizabilities ($\beta = \beta_{tot}$, in a.u.) of compounds **D1-D4** , calculated at the TD-DFT/M06-2X level using different basis sets. The geometries of the compounds have been optimized at the IEF-PCM/M06-2X/6-311+G(d) level.

Three basis set used for describing the iodide counterion were also evaluated, by calculating the static first hyperpolarizability of the **D3**/iodide complex. In these tests the 6-311+G(d) basis set was used for the dye. The results collected in Table S5 show that varying the basis set for iodine atom does not impact significantly the values of $\beta$.

Table S5: Static first hyperpolarizabilities ($\beta_{tot}$, in $10^4$ a.u.) of the **D3**/iodide complex as a function of the basis set used for describing the iodide anion (by using geometries optimized at the IEF-PCM/M06-2X/6-311+G(d) level). These computations have been performed on 24 cpus on a Xeon node with 64 Gb of RAM. The total number $N_{basis}$ of basis functions and the computation time (min) are also provided.

| Dye basis | Iodine basis | $\beta_{tot}$ | $N_{basis}$ | Time |
|---|---|---|---|---|
| 6-311+G(d) | 6-311G(d) | 16.1 | 857 | 18 |
| 6-311+G(d) | aug-cc-pvdz(PP) | 16.1 | 827 | 18 |
| 6-311+G(d) | aug-cc-pvtz(PP) | 16.1 | 850 | 32 |

# 6 Optimized structures of the dye/iodide complexes

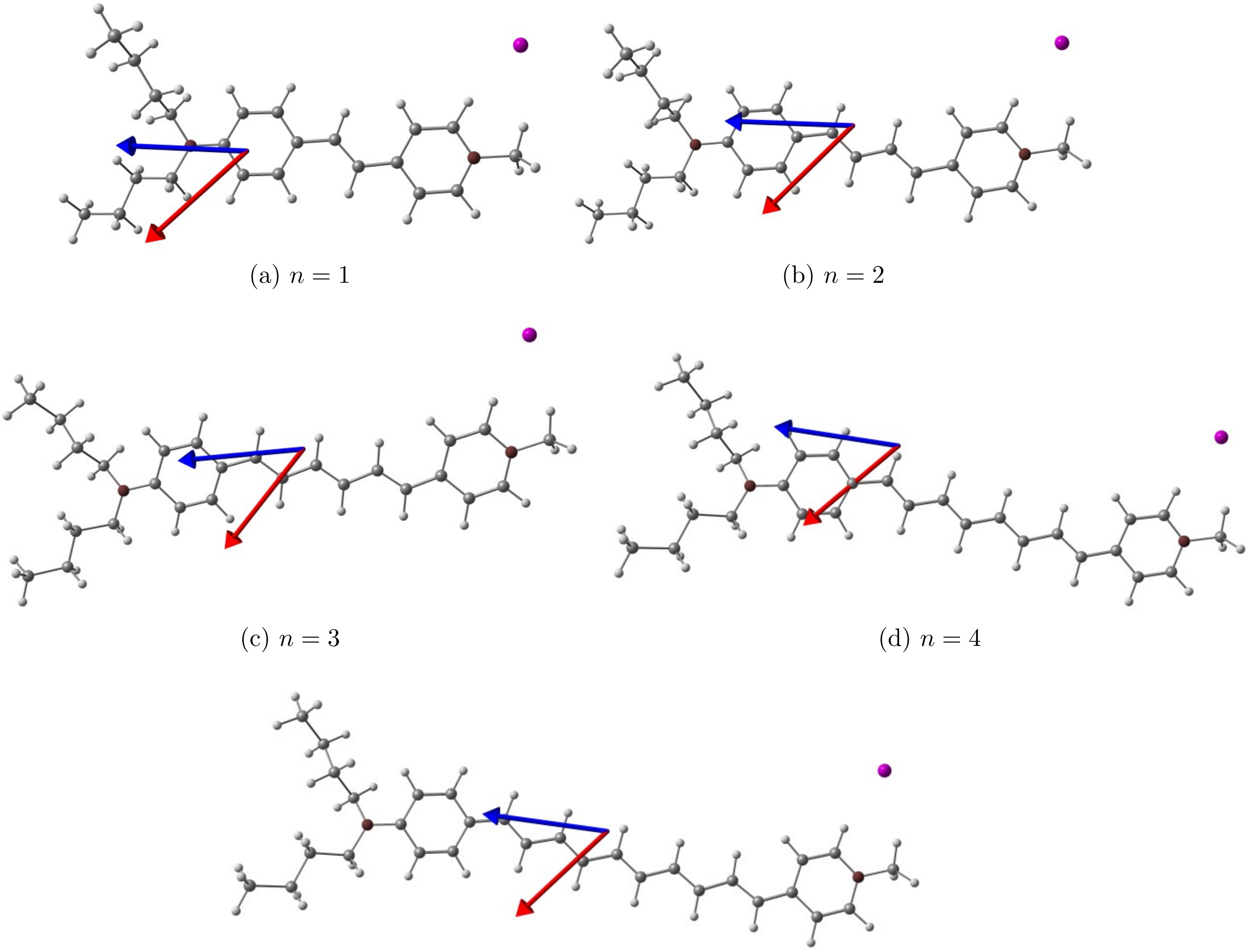

(a) $n = 1$

(b) $n = 2$

(c) $n = 3$

(d) $n = 4$

(e) $n = 5$

Figure S17: Optimized structures of the dye/iodide complexes for dyes of series **A** with the orientation of the (normalized) $\vec{\mu}$ (red) and $\vec{\beta}$ (blue) vectors.

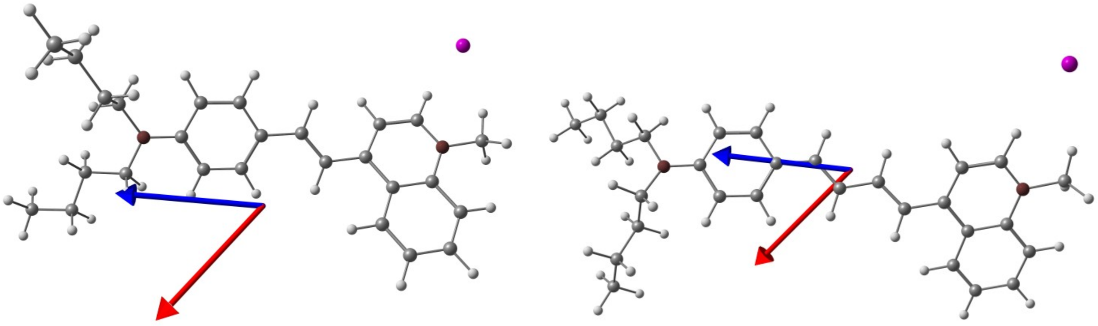

(a) $n = 1$ (b) $n = 2$

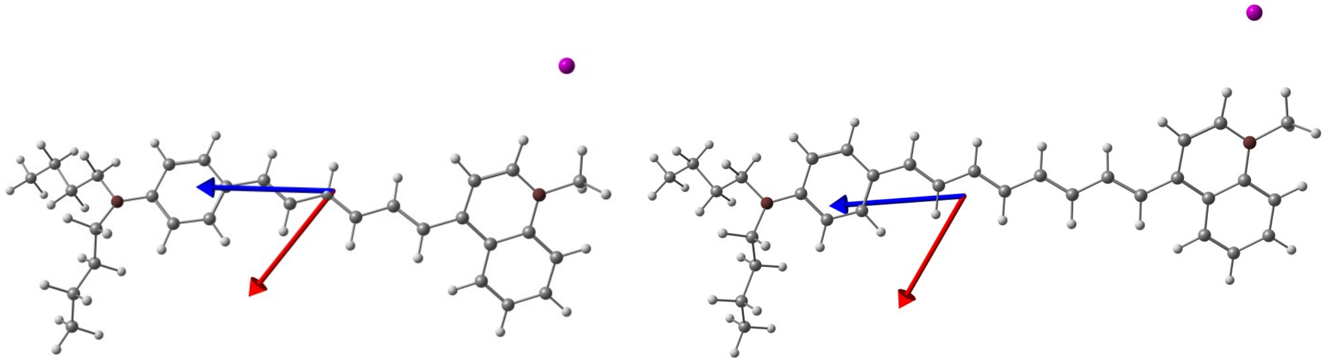

(c) $n = 3$ (d) $n = 4$

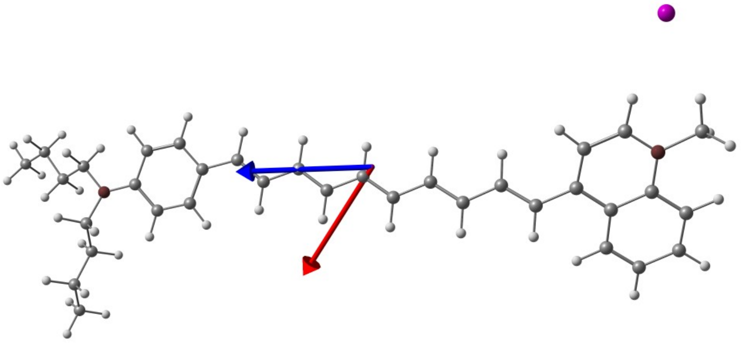

(e) $n = 5$

Figure S18: Optimized structures of the dye/iodide complexes for dyes of series **B** with the orientation of the (normalized) $\vec{\mu}$ (red) and $\vec{\beta}$ (blue) vectors.

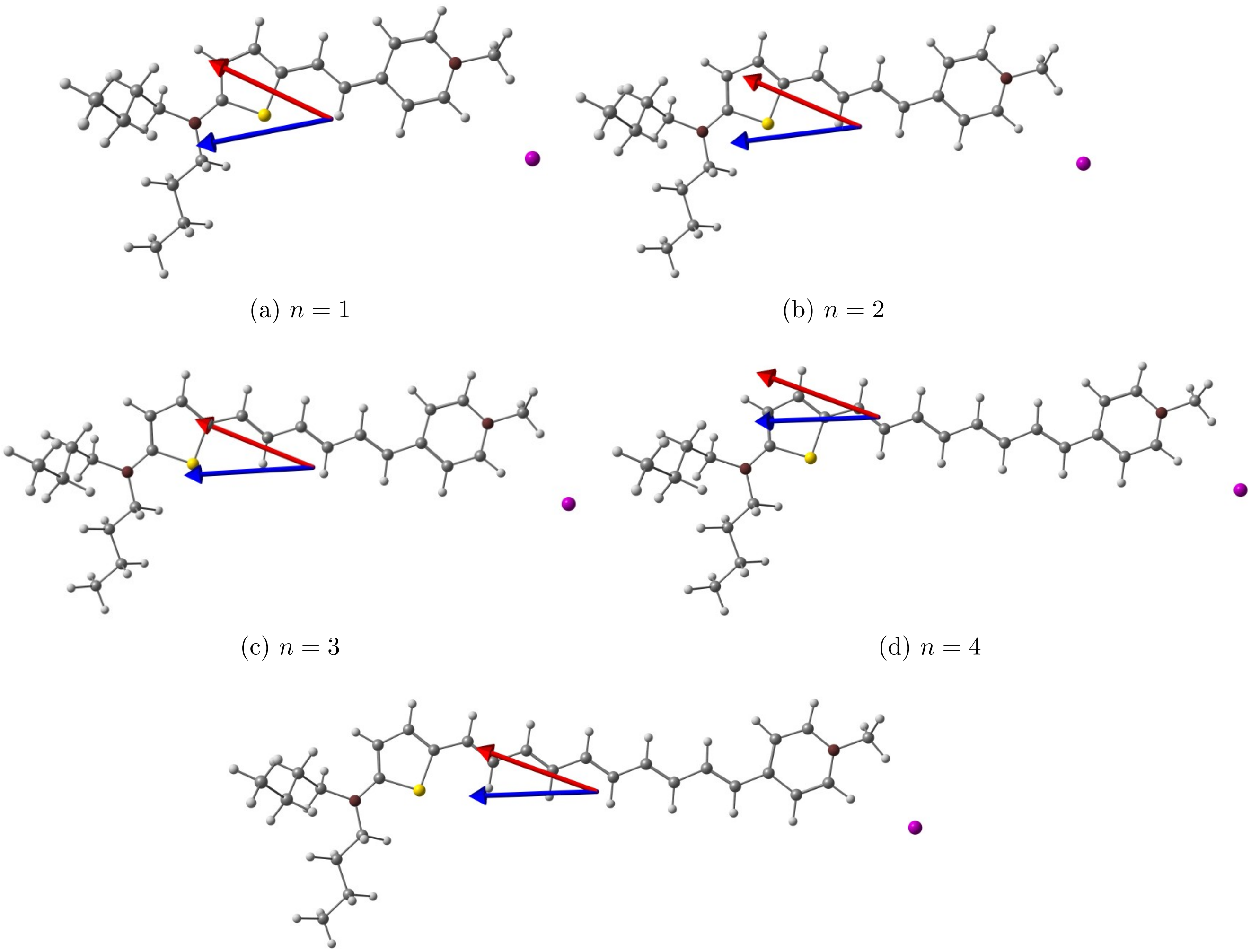

(a) $n = 1$

(b) $n = 2$

(c) $n = 3$

(d) $n = 4$

(e) $n = 5$

Figure S19: Optimized structures of the dye/iodide complexes for dyes of series **C** with the orientation of the (normalized) $\vec{\mu}$ (red) and $\vec{\beta}$ (blue) vectors.

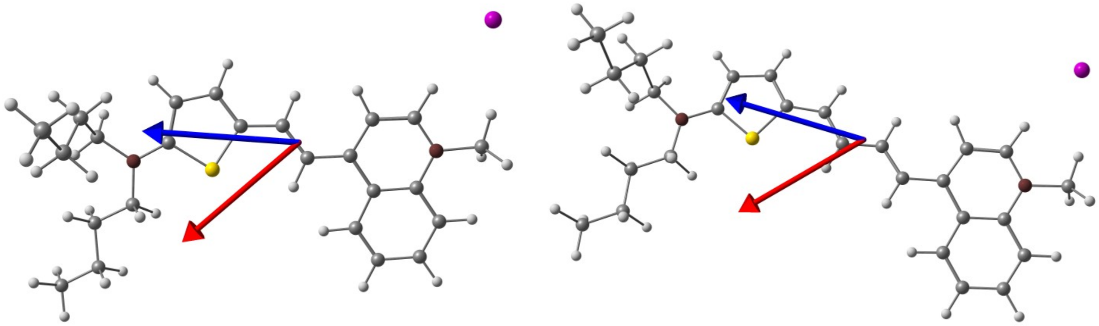

(a) $n = 1$ (b) $n = 2$

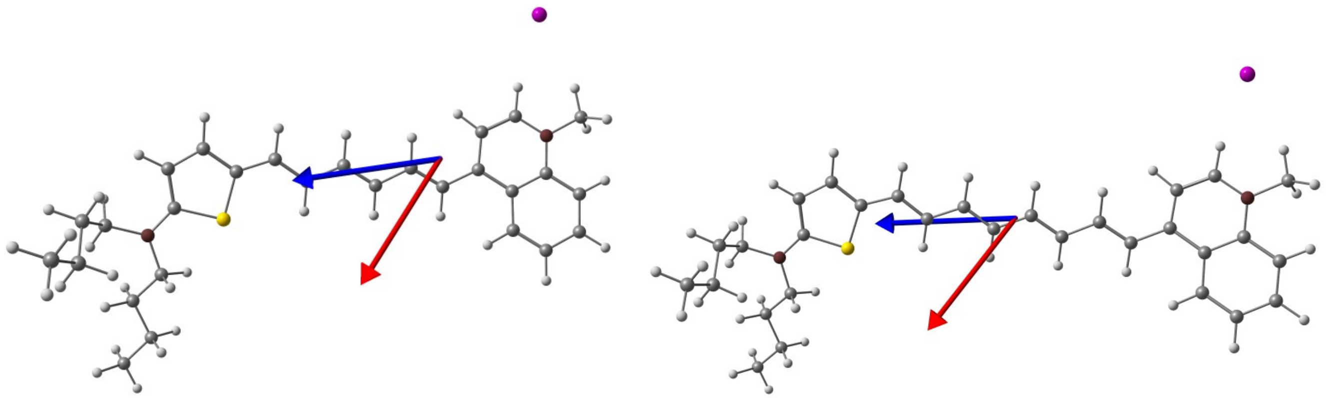

(c) $n = 3$ (d) $n = 4$

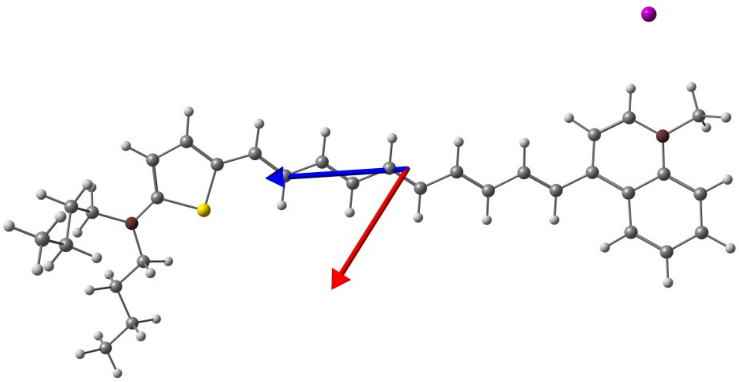

(e) $n = 5$

Figure S20: Optimized structures of the dye/iodide complexes for dyes of series **D** with the orientation of the (normalized) $\vec{\mu}$ (red) and $\vec{\beta}$ (blue) vectors.

# 7 Correlation between hyperpolarizabilities and aromaticity indices in dye/iodide complexes

Table S6: Bond order alternation (BOA) and aromaticity indices (FLU and $AV_{\text{min}}$ ) computed along the conjugated linker between donors and acceptors. Atoms included in the calculation of the indices are reported in Figure S21.

| Molecule | BOA | FLU | $AV_{\text{min}}$ |
|---|---|---|---|
| **A1** | 0.4706 | 0.0312 | — |
| **A2** | 0.4383 | 0.0273 | 1.7750 |
| **A3** | 0.4341 | 0.0264 | 1.5480 |
| **A4** | 0.4370 | 0.0263 | 1.4550 |
| **A5** | 0.4388 | 0.0263 | 1.4010 |
| **B1** | 0.4705 | 0.0314 | — |
| **B2** | 0.4293 | 0.0264 | 1.8110 |
| **B3** | 0.4299 | 0.0260 | 1.5530 |
| **B4** | 0.4292 | 0.0256 | 1.4680 |
| **B5** | 0.4368 | 0.0261 | 1.3970 |
| **C1** | 0.3416 | 0.0174 | — |
| **C2** | 0.3537 | 0.0180 | 2.6400 |
| **C3** | 0.3747 | 0.0195 | 2.2400 |
| **C4** | 0.3935 | 0.0211 | 2.0430 |
| **C5** | 0.4080 | 0.0223 | 1.9050 |
| **D1** | 0.2814 | 0.0126 | — |
| **D2** | 0.3092 | 0.0142 | 2.8660 |
| **D3** | 0.3400 | 0.0164 | 2.3880 |
| **D4** | 0.3757 | 0.0193 | 2.1090 |
| **D5** | 0.3920 | 0.0207 | 1.9540 |

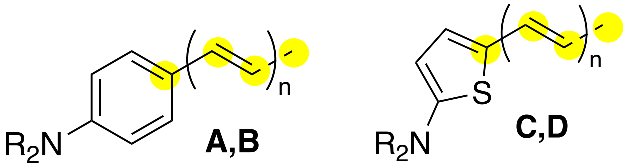

Figure S21: Atoms included in the calculation of indices reported in Table S6.

Table S7: Aromaticity indices ( MCI, $I_{ring}$, FLU, and $AV_{\mathrm{min}}$ ) within the phenyl ring (in series **A** and **B**) and thienyl ring (in series **C** and **D**). Atoms included in the calculation of the indices are reported in Figure S22. The values of the same indicators for the benzene and thiophene molecules optimized at the same level of theory are reported for comparison.

| Molecule | MCI | $I_{ring}$ | FLU | $AV_{\mathrm{min}}$ |
|---|---|---|---|---|
| **A1** | 0.0431 | 0.0305 | 0.0071 | 4.9180 |
| **A2** | 0.0445 | 0.0314 | 0.0064 | 5.2800 |
| **A3** | 0.0458 | 0.0321 | 0.0058 | 5.5970 |
| **A4** | 0.0467 | 0.0327 | 0.0054 | 5.8220 |
| **A5** | 0.0472 | 0.0329 | 0.0052 | 5.9390 |
| **B1** | 0.0431 | 0.0306 | 0.0071 | 4.9190 |
| **B2** | 0.0444 | 0.0313 | 0.0065 | 5.2360 |
| **B3** | 0.0458 | 0.0322 | 0.0059 | 5.5890 |
| **B4** | 0.0466 | 0.0326 | 0.0055 | 5.7810 |
| **B5** | 0.0473 | 0.0330 | 0.0052 | 5.9700 |
| **C1** | 0.0187 | 0.0172 | 0.0068 | — |
| **C2** | 0.0191 | 0.0174 | 0.0067 | — |
| **C3** | 0.0194 | 0.0175 | 0.0068 | — |
| **C4** | 0.0196 | 0.0175 | 0.0070 | — |
| **C5** | 0.0198 | 0.0175 | 0.0072 | — |
| **D1** | 0.0179 | 0.0169 | 0.0072 | — |
| **D2** | 0.0186 | 0.0172 | 0.0068 | — |
| **D3** | 0.0191 | 0.0174 | 0.0068 | — |
| **D4** | 0.0195 | 0.0175 | 0.0070 | — |
| **D5** | 0.0197 | 0.0175 | 0.0072 | — |
| **Benzene** | 0.0744 | 0.0494 | 0.0000 | 10.9270 |
| **Thiophene** | 0.0393 | 0.0302 | 0.0095 | — |

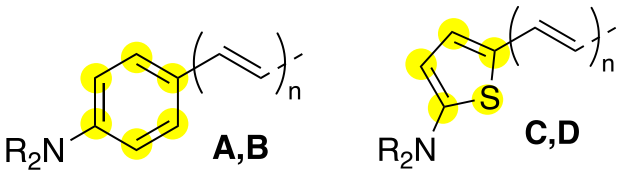

Figure S22: Atoms included in the calculation of indices reported in Table S7.

Table S8: Bond length alternation (BLA), Bond order alternation (BOA) and aromaticity indices (FLU and $AV_{\mathrm{min}}$ ) computed along the conjugated path going from the amine nitrogen to the first carbon of the pyridinium (series **A** and **B**) or quinolinium (series **C** and **D**). Atoms included in the calculation of the indices are reported in Figure S23.

| Molecule | BLA | BOA | FLU | $AV_{\mathrm{min}}$ |
|---|---|---|---|---|
| **A1** | -0.0189 | 0.1021 | 0.0180 | 1.1390 |
| **A2** | -0.0359 | 0.2109 | 0.0187 | 0.9960 |
| **A3** | -0.0467 | 0.2587 | 0.0197 | 0.9350 |
| **A4** | -0.0545 | 0.2930 | 0.0206 | 0.8500 |
| **A5** | -0.0600 | 0.3190 | 0.0212 | 0.8460 |
| **B1** | -0.0206 | 0.1463 | 0.0176 | 1.2500 |
| **B2** | -0.0372 | 0.2190 | 0.0177 | 1.0760 |
| **B3** | -0.0484 | 0.2675 | 0.0190 | 0.9320 |
| **B4** | -0.0550 | 0.2967 | 0.0197 | 0.8530 |
| **B5** | -0.0610 | 0.3233 | 0.0209 | 0.7790 |
| **C1** | -0.0219 | 0.1735 | 0.0085 | 1.3430 |
| **C2** | -0.0379 | 0.2373 | 0.0109 | 1.1500 |
| **C3** | -0.0493 | 0.2844 | 0.0133 | 0.9850 |
| **C4** | -0.0575 | 0.3192 | 0.0154 | 0.8530 |
| **C5** | -0.0634 | 0.3444 | 0.0172 | 0.7570 |
| **D1** | -0.0132 | 0.1304 | 0.0065 | 1.5100 |
| **D2** | -0.0311 | 0.2035 | 0.0087 | 1.2740 |
| **D3** | -0.0438 | 0.2572 | 0.0112 | 1.0780 |
| **D4** | -0.0547 | 0.3053 | 0.0142 | 0.8930 |
| **D5** | -0.0609 | 0.3317 | 0.0160 | 0.7880 |

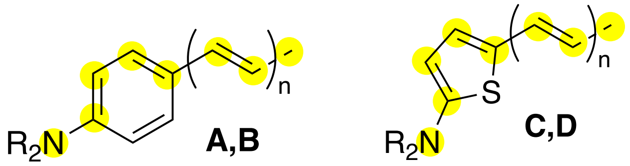

Figure S23: Atoms included in the calculation of indices reported in Table S8

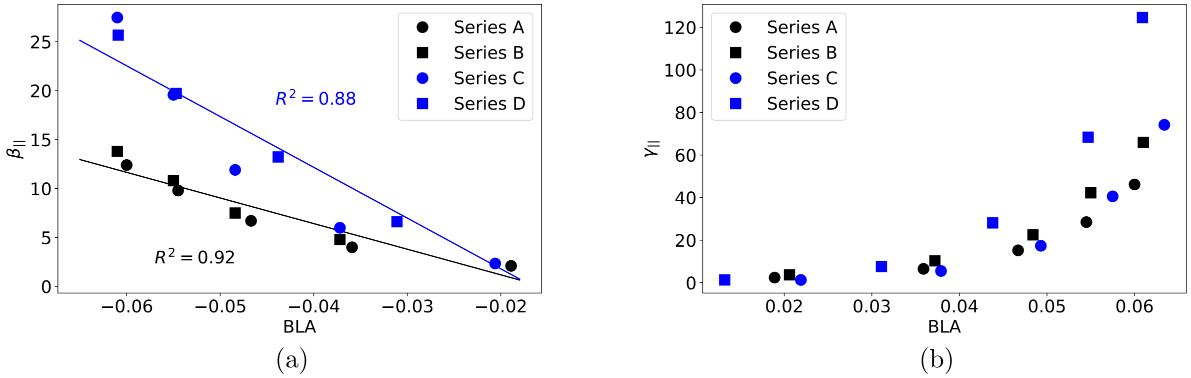

(a) (b)

Figure S24: Evolution of $\beta_{||}$ ($10^4$ a.u.) and $\gamma_{||}$ ($10^6$ a.u.) as a function of the BLA computed along the conjugated path going from the amine nitrogen to the first carbon of the pyridinium (series **A** and **B**) or quinolinium (series **C** and **D**). Atoms included in the calculation of the indices are reported in Figure S23.

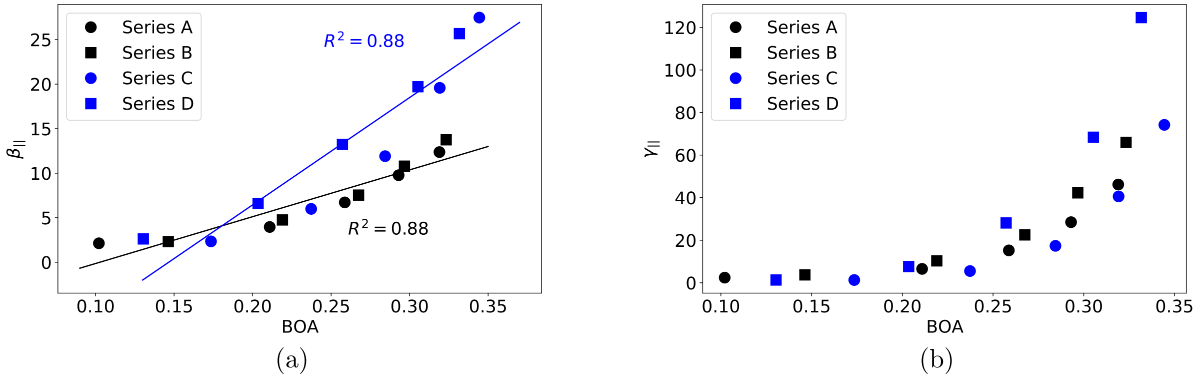

(a) (b)

Figure S25: Evolution of $\beta_{||}$ ($10^4$ a.u.) and $\gamma_{||}$ ($10^6$ a.u.) as a function of the BOA computed along the polyenic bridge. Atoms included in the calculation of the indices are reported in Figure S23.

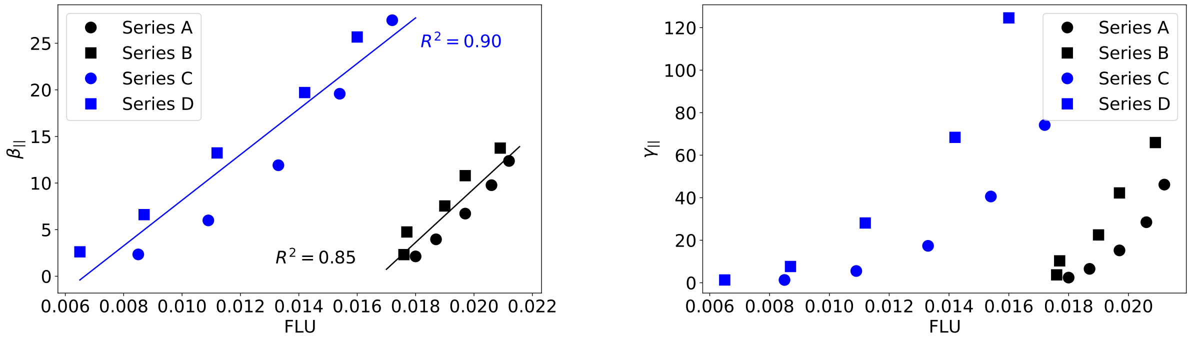

(a) (b)

Figure S26: Evolution of $\beta_{||}$ ($10^4$ a.u.) and $\gamma_{||}$ ($10^6$ a.u.) as a function of the FLU computed along the conjugated path going from the amine nitrogen to the first carbon of the pyridinium (series **A** and **B**) or quinolinium (series **C** and **D**). Atoms included in the calculation of the indices are reported in Figure S23.

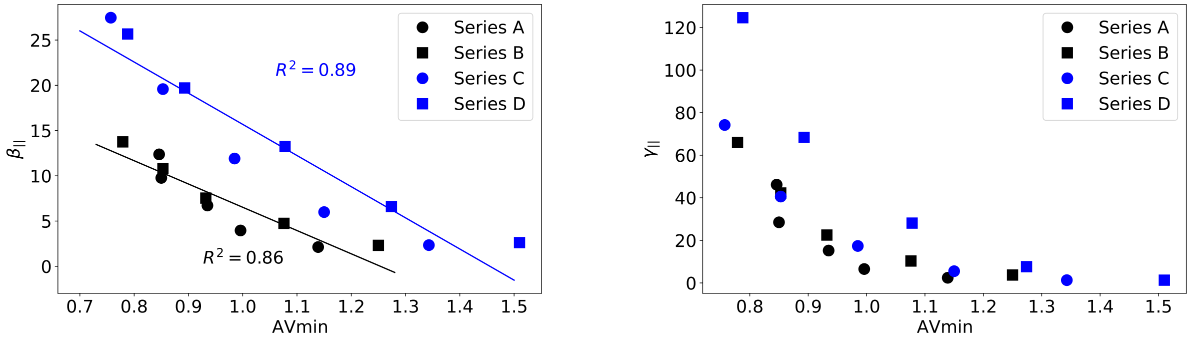

(a) (b)

Figure S27: Evolution of $\beta_{||}$ ($10^4$ a.u.) and $\gamma_{||}$ ($10^6$ a.u.) as a function of the $AV_{\text{min}}$ computed along the conjugated path going from the amine nitrogen to the first carbon of the pyridinium (series **A** and **B**) or quinolinium (series **C** and **D**). Atoms included in the calculation of the indices are reported in Figure S23.

# 8 Aromaticity and conjugation measures

The present section will briefly review the conjugation and aromaticity indices used in the manuscript. The latter have been adapted to study the conjugated chains in series **A-B** and **C-D**. From now on, we will use the abbreviated notation $\mathbf{1} \equiv (\vec{r}_1, \sigma_1)$ to represent the coordinates of an electron, and $d\mathbf{1} \equiv d\vec{r}_1, d\sigma_1$ to represent the electron positions and their derivatives. In order to provide a general expression, we will consider a molecule that includes at least one ring structure composed of $n$ atoms, which is represented by the sequence $\mathcal{A} = \{A_1, A_2, \ldots, A_n\}$. The elements of this sequence are ordered in accordance with the convention that the first atom in the sequence, $A_1$, is adjacent to the last atom, $A_n$, forming a ring.

Apart from the bond-length alternation (BLA), in this work, we have considered another *geometric* measure of conjugation, the harmonic oscillator model of aromaticity (HOMA),[S2] defined as

$$HOMA(\mathcal{A}) = 1 - \frac{1}{n-1}\sum_{i}^{n-1} \alpha_i (R_{opt} - r_{A_i,A_{i+1}})^2, \tag{2}$$

where $r_{A,B}$ is the distance between atoms $A$ and $B$, and $\alpha_i$ is an empirical constant optimized to give values close to one for aromatic species and small or negative values for non-aromatic and antiaromatic species. The geometrical data of reference ($R_{opt}$) is such that the compression energy of the double bond and the expansion energy of the single bond is minimal in accordance with the harmonic potential model. Although originally defined for rings,[S2,S3] HOMA can be easily adapted to open fragments, as we did in Eq. 2.

The other measures considered in the manuscript are based on the electron delocalization between atoms. In order to define these measures, we rely on two indices defined in the framework of the quantum theory of atoms-in-molecules (QTAIM).[S4] The delocalization index (DI)[S5–S7] measures the number of electrons fluctuating concurrently between two atoms

$A_1$ and $A_2$, and is defined as

$$\delta(A_1, A_2) = 2 \int_{A_1} \int_{A_2} d\mathbf{1}d\mathbf{2}\rho_{xc}(\mathbf{1}, \mathbf{2}) = -2cov(N_{A_1}, N_{A_2}), \tag{3}$$

where $N_{A_1}$ and $N_{A_2}$ are the atomic populations and $\rho_{xc}(\mathbf{1}, \mathbf{2})$ is the exchange–correlation density (XCD). The localization index (LI) is defined as

$$\lambda(A) = \int_{A} \int_{A} d\mathbf{1}d\mathbf{2}\rho_{xc}(\mathbf{1}, \mathbf{2}), \tag{4}$$

where we integrate the two points of the XCD over the same atom $A$.

The bond-order alternation (BOA)[S8] measures the electron delocalization difference between consecutive atoms and it is defined after BLA, but replacing bond lengths by bond orders (in this case, we use the DIs):

$$BOA(\mathcal{A}) = \frac{1}{N-2} \sum_{i=1}^{N-2} (-1)^{i+1} [\delta(A_{i+1}, A_{i+2}) - \delta(A_i, A_{i+1})] \tag{5}$$

The aromatic fluctuation index (FLU) is the counterpart to HOMA and measures electron delocalization differences with respect to some aromatic references. In the present case it is defined as

$$FLU(\mathcal{A}) = \frac{1}{n} \sum_{i=1}^{n} \left[ \left( \frac{\delta(A_i)}{\delta(Ai-1)} \right)^{\alpha} \left( \frac{\delta(A_i, A_{i-1}) - \delta_{ref}(A_i, A_{i-1})}{\delta_{ref}(A_i, A_{i-1})} \right) \right]^2, \tag{6}$$

where $\alpha$ ensures the first term is always greater or equal to 1,

$$\alpha \begin{cases} 1 & \delta(A_{i-1}) \leq \delta(A_i) \\ -1 & \delta(A_i) < \delta(A_{i-1}) \end{cases} \tag{7}$$

and $\delta_{ref}(A, B)$ is the DI of an aromatic molecule of reference. Benzene is used as a reference for C-C bonds, the C-N value is taken from pyridine, and the C-S value is taken from thiophene.[S9] When the molecule is aromatic, the FLU index will be close to zero, whereas for non-aromatic or antiaromatic species, it will be greater than zero. Aromaticity indicators based on bond orders, such as BLA or FLU, do not strongly depend on the computational method used.[S10]

Giambiagi employed one of the most reliable electronic multicenter indices as an aromaticity index. $I_{ring}$ measures the delocalization along the ring:[S11]

$$I_{ring}(\mathcal{A}) = \sum_{i_1 i_2 \ldots i_n}^{occ} S_{i_1 i_2}(A_1) S_{i_2 i_3}(A_2) \ldots S_{i_n, i_1}(A_n), \tag{8}$$

where $S_{ij}(A)$ stands for the overlaps of molecular orbitals $i$ and $j$ in the molecular region occupied by atom $A$. If one takes into account all the permutations of the atoms in the ring, including delocalization patterns across the ring, we obtain the expression of the multicenter index (MCI):[S12]

$$MCI(\mathcal{A}) = \frac{1}{2n} \sum_{\mathcal{P}(\mathcal{A})} I_{ring}(\mathcal{A}) = \frac{1}{2n} \sum_{\mathcal{P}(\mathcal{A})} \sum_{i_1 i_2 \ldots i_n}^{occ} S_{i_1 i_2}(A_1) S_{i_2 i_3}(A_2) \ldots S_{i_n, i_1}(A_n) \tag{9}$$

where $\mathcal{P}(\mathcal{A})$ stands for the $n!$ permutations of the elements in the string $\mathcal{A}$. Like $I_{ring}$, MCI gives large numbers for aromatic species, and the authors claim negative values for antiaromatic molecules.[S13] However, these two electronic indices are not suitable for large (anti)aromatic molecules because they scale exponentially with the number of atoms in the ring and present large numerical errors derived from the numerical integration of the atomic overlap matrices.

In order to solve the drawbacks of $I_{ring}$ and MCI, we have defined the AV1245 index[S14] as the average value of the four-atom MCI index between relative positions 1-2 and 4-5 constructed from every five consecutive atoms along the perimeter of the ring. Lately,[S15,S16] it has been seen that the average value could hinder some important values and that the minimal value of the index, $AV_{\min}$ , could be more appropriate. The $AV_{\min}$ value corresponds to the least delocalized fragment of the ring. Aromatic molecules (and conjugated fragments) present large values of $AV_{\min}$ , while non-aromatic molecules (and non-conjugated fragments) exhibit low values.

# References

(S1) Parthasarathy, V.; Pandey, R.; Stolte, M.; Ghosh, S.; Castet, F.; Würthner, F.; Das, P. K.; Blanchard-Desce, M. Combination of Cyanine Behaviour and Giant Hyperpolarisability in Novel Merocyanine Dyes: Beyond the Bond Length Alternation (BLA) Paradigm. *Chem. Eur. J.* **2015**, *21*, 14211–14217.

(S2) Kruszewski, J.; Krygowski, T. M. Definition of aromaticity basing on the harmonic oscillator model. *Tetrahedron Lett.* **1972**, *13*, 3839–3842.

(S3) Cyranski, M. K. Energetic aspects of cyclic pi-electron delocalization: evaluation of the methods of estimating aromatic stabilization energies. *Chem. Rev.* **2005**, *105*, 3773–3811.

(S4) Bader, R. F. W. *Atoms in Molecules: A Quantum Theory*; Oxford University Press: Oxford, 1990.

(S5) Bader, R. F. W.; Stephens, M. E. Spatial localization of the electronic pair and number distributions in molecules . *J. Am. Chem. Soc.* **1975**, *97*, 7391–7399.

(S6) Fradera, X.; Austen, M. A.; Bader, R. F. W. The Lewis Model and Beyond. *J. Phys. Chem. A* **1999**, *103*, 304–314.

(S7) Matito, E.; Solà, M.; Salvador, P.; Duran, M. Electron sharing indexes at the correlated level. Application to aromaticity calculations. *Faraday Discuss.* **2007**, *135*, 325–345.

(S8) Casademont-Reig, I.; Ramos-Cordoba, E.; Torrent-Sucarrat, M.; Matito, E. How do the Hückel and Baird Rules Fade away in Annulenes? *Molecules* **2020**, *25*, 711.

(S9) Matito, E.; Duran, M.; Solà, M. The aromatic fluctuation index (FLU): a new aromaticity index based on electron delocalization. *J. Chem. Phys.* **2005**, *122*, 014109.

(S10) Matito, E.; Solà, M.; Duran, M.; Salvador, P. Aromaticity Measures from Fuzzy-Atom Bond Orders (FBO). The Aromatic Fluctuation (FLU) and the para-Delocalization (PDI) Indexes. *J. Phys. Chem. A* **2006**, *110*, 5108–5113.

(S11) Giambiagi, M.; de Giambiagi, M. S.; dos Santos Silva, C. D.; de Figuereido, A. P. Multicenter bond indices as a measure of aromaticity. *Phys. Chem. Chem. Phys.* **2000**, *2*, 3381–3392.

(S12) Bultinck, P.; Ponec, R.; Van Damme, S. Multicenter bond indices as a new measure of aromaticity in polycyclic aromatic hydrocarbons. *J. Phys. Org. Chem.* **2005**, *18*, 706–718.

(S13) Ponec, R.; Bultinck, P.; Saliner, A. G. Multicenter bond indices as a new means for the quantitative characterization of homoaromaticity. *J. Phys. Chem. A* **2005**, *109*, 6606.

(S14) Matito, E. Electronic Aromaticity Index for Large Rings. *Phys. Chem. Chem. Phys.* **2016**, *18*, 11839–11846.

(S15) Casademont-Reig, I.; Woller, T.; Contreras-García, J.; Alonso, M.; Torrent-Sucarrat, M.; Matito, E. New electron delocalization tools to describe the aromaticity in porphyrinoids. *Phys. Chem. Chem. Phys.* **2018**, *20*, 2787–2796.

(S16) García-Fernández, C.; Sierda, E.; Abadia, M.; Bugenhagen, B. E. C.; Prosenc, M. H.; Wiesendanger, R.; Bazarnik, M.; Ortega, J. E.; Brede, J.; Matito, E.; Arnau, A. Exploring the Relation Between Intramolecular Conjugation and Band Dispersion in One-Dimensional Polymers. *J. Phys. Chem. C* **2017**, *121*, 27118–27125.